Cement & Concrete Composites 33 (2011) 881–890

Contents lists available at ScienceDirect

Cement & Concrete Composites

journal homepage: www.elsevier.com/locate/cemconcomp

Lattice Discrete Particle Model (LDPM) for failure behavior of concrete. I: Theory

Gianluca Cusatis [a,*], Daniele Pelessone [b], Andrea Mencarelli [a]

[a] Department of Civil and Environmental Engineering, Rensselaer Polytechnic Institute, Troy, NY 12180, USA
[b] Engineering and Software System Solutions, Inc. (ES3), San Diego, CA 92101, USA

ARTICLE INFO

Article history:
Received 14 November 2010
Received in revised form 12 February 2011
Accepted 14 February 2011
Available online 19 February 2011

Keywords:
Concrete
Fracture
Failure
Discrete models
Lattice models
Particle models
Calibration
Validation

ABSTRACT

This paper deals with the formulation, calibration, and validation of the Lattice Discrete Particle Model (LDPM) suitable for the simulation of the failure behavior of concrete. LDPM simulates concrete at the meso-scale considered to be the length scale of coarse aggregate pieces. LDPM is formulated in the framework of discrete models for which the unknown displacement field is not continuous but only defined at a finite number of points representing the center of aggregate particles. Size and distribution of the particles are obtained according to the actual aggregate size distribution of concrete. Discrete compatibility and equilibrium equations are used to formulate the governing equations of the LDPM computational framework. Particle contact behavior represents the mechanical interaction among adjacent aggregate particles through the embedding mortar. Such interaction is governed by meso-scale constitutive equations simulating meso-scale tensile fracturing with strain-softening, cohesive and frictional shearing, and nonlinear compressive behavior with strain-hardening. The present, Part I, of this two-part study deals with model formulation leaving model calibration and validation to the subsequent Part II.

1. Introduction

Concrete is a heterogeneous material characterized by several length scales of observation ranging from the length scale of crystalline particles of hydrated Portland cement (10^{-9} m) to the macroscopic scale (10^{1} m), at which concrete has been traditionally considered homogeneous. It is now widely recognized that accurate modeling of multiscale materials calls for the adoption of multiscale techniques able to bridge the various scales and to bring to the macroscopic scale the most important effects of lower scale phenomena. In the recent past, publications proposing new multiscale theories have flourished, especially for modeling nano-composite materials and atomistic and molecular systems [23]. The same kind of development has not appeared yet in concrete mechanics literature or in civil engineering in general. The main reason for this can be traced back to the extreme complexity of concrete internal structure and to the unavailability of accurate fine-scale models for concrete.

In the last twenty years, various authors attempted the development of concrete models targeting concrete mini-scale (length scale of 10^{-4} m or less) and meso-scale (length scale 10^{-3} m). The term "mini-scale" was first introduced by Cusatis et al. [18] and is relevant to the description of concrete as a three-phase material: cement paste, aggregate, and interfacial transitional zone, whereas the meso-scale is relevant to the characterization of concrete as two-phase material: mortar and coarse aggregate. It must be noted that some authors use the term "meso-scale" in a wider sense to include the "mini-scale".

Mini-scale models were proposed by several authors [29,30,10,1,9,33]. Remarkable are the contributions due to Wittmann and coworkers [29] for 2D models, and to Carol and coworkers [12,11,13] for 3D models. They used finite element techniques to model, with different constitutive laws, coarse aggregate pieces, mortar matrix, and an inclusion-matrix interface. This led to very large computational systems characterized by several thousands of degrees of freedom even for the simulation of small specimens. An alternative to the use of finite elements was proposed by Van Mier and coworkers [30] who removed the continuum hypothesis and modeled concrete through a discrete system of beams (lattice). In their approach, lattice meshes were superimposed to digitalized images of the concrete internal structure to assign different material properties to the lattice elements corresponding to the various components (matrix, aggregate, and interface). Along this line, Bolander and coworkers [9,33] formulated a discrete mini-scale model based on the interaction between rigid polyhedral particles obtained though the Voronoi tessellation of the domain. Similar approach was used by Nagai et al. [26] to simulate mortar and

* Corresponding author. Address: Department of Civil and Environmental Engineering, 4048 Johnsson Engineering Center, Rensselaer Polytechnic Institute, 110 Eighth St, Troy, NY 12180-3590, USA. Tel.: +1 518 276 3956; fax: +1 518 276 4833.

E-mail addresses: cusatg@rpi.edu (G. Cusatis), peless@es3inc.com (D. Pelessone), mencaa@rpi.edu (A. Mencarelli).

0958-9465/$ - see front matter © 2011 Elsevier Ltd. All rights reserved.
doi:10.1016/j.cemconcomp.2011.02.011

concrete in a 2D setting. Mini-scale models provide realistic simulations of concrete cracking, coalescence of multiple distribute cracks into localized cracks, and fracture propagation. However, they tend to be computationally intensive, especially for 3D modeling that is required to correctly capture compressive failure and confinement effects.

Computationally less demanding are the meso-scale models [5,16,18] in which the basic material components, whole aggregate pieces and the layer of mortar matrix between them, are modeled through discrete elements (either lattice elements or discrete particles) but are themselves not discretized on a finer scale. Meso-scale models greatly reduce the size of the numerical problems but at the same time can capture the fundamental aspects of material heterogeneity. Meso-scale models have made possible the realistic simulation of both tensile and compressive softening. Preliminary results on the modeling of multiaxial behavior and confinement effects were also achieved by Cusatis et al. [17] and Belheine et al. [7].

The main objective of this article is to discuss a recently developed meso-scale model for concrete, called the Lattice Discrete Particle Model (LDPM). The development of LDPM is a synthesis of two independent research efforts that led to the formulation of the Confinement Shear Lattice (CSL) Model [18,16,17] and the Discrete Particle Model (DPM) [27].

LDPM shares the following features with CSL: (a) it simulates concrete mesostructure by a system of interacting aggregate particles connected by a lattice system that is obtained through a Delaunay tetrahedralization of the aggregate centers; (b) the position of each aggregate piece throughout a given concrete specimen is defined by means of the basic concrete properties and the size distribution of the aggregates; (c) the geometry of the lattice struts connecting adjacent particles is obtained by a three-dimensional domain tessellation defining a set of polyhedral cells each including one aggregate piece; (d) the mechanical interaction between the particles is characterized by both normal and shear stresses; and (e) the meso-scale constitutive behavior is softening for pure tension and shear-tension while it is plastic hardening for pure compression and shear-compression.

LDPM inherited from DPM the Modeling and Analysis of the Response of Structures (MARS) computational environment [28] that includes long range contact capabilities typical of the classical formulation of Discrete Element Methods (DEM) [15]. This feature is particularly important for simulating pervasive failure and fragmentation.

While building on the successful developments of CSL and DPM, LDPM formulation is characterized by a number of new features that greatly enhance its modeling and predictive capabilities. These new features can be summarized as follows:

1. Interaction among the particles is formulated through the analysis of an assemblage of four aggregate pieces whose centers are the vertexes of the Delaunay tetrahedralization. This makes possible the inclusion of volumetric effects in the constitutive law that cannot be taken into account by the two particle interaction used in CSL and DPM.
2. Stresses and strains are defined at each single facet of the polyhedral cells containing the aggregate pieces. Compared to previous formulations, this allows a better stress resolution in the mesostructure, which, in turn, leads to a better representation of meso-scale crack and damage distribution.
3. The constitutive law simulates the most relevant physical phenomena governing concrete damage and failure under tension as well as compression. Compared to the constitutive law used in the previous work [16], the present law provides better modeling and predictive capabilities especially for the macroscopic behavior in compression with confinement effects.
4. The constitutive equations include simple but effective unloading-reloading rules that permit an accurate simulation of concrete response under cyclic loadings.
5. The constitutive equations also include the effect of material compaction and densification due to the effect of high confining pressures.

The present formulation can realistically simulate all aspects of concrete response under quasi-static loading, including tensile and compressive strength, cohesive fracture and size effect, damage in compression, compression-shear behavior with softening at zero or low-confinement and hardening at high confined compression, and strength increase under biaxial loading. This paper (Part I of a two-part study) discusses the details of LDPM formulation and its numerical implementation. Part II will focus on its extensive calibration and validation.

2. Geometrical characterization of concrete mesostructure

The geometrical characterization of concrete mesostructure is based on a four-step procedure that aims at defining (1) the number and size of coarse aggregate pieces (particles); (2) particle position; (3) interparticle connections; and (4) surfaces through which forces are transmitted between adjacent particles. These surfaces will also represent weak locations in the concrete mesostructure, where damage is likely to localize.

2.1. Particle generation

In the first step, particle generation is carried out by assuming that each aggregate piece can be approximated as a sphere. Under this assumption, typical concrete granulometric distributions can be represented by the particle size distribution function (psd) proposed by Stroeven [32]:

$$f(d) = \frac{q d_0^q}{[1-(d_0/d_a)^q] d^{q+1}} \tag{1}$$

where d_a is the maximum aggregate size, and d_0 is the minimum particle size used in the simulations, and q is a material parameter. It must noted here that, in general, $d_0 \neq 0$ to limit the number of degrees of freedom to be solved in the numerical simulations. The above psd can be interpreted as the probability density function (pdf) for the occurrence of a certain diameter d. The cumulative distribution function (cdf) can be then computed as

$$P(d) = \int_{d_0}^{d} f(d)\mathrm{d}d = \frac{1-(d_0/d)^q}{1-(d_0/d_a)^q} \tag{2}$$

It can be shown [32] that the psd in Eq. (1) is associated with a sieve curve (percentage of aggregate by weight retained by a sieve of characteristic size d) in the form

$$F(d) = \left(\frac{d}{d_a}\right)^{n_F} \tag{3}$$

where $n_F = 3 - q$. For $q = 2.5$ ($n_F = 0.5$), Eq. (3) corresponds to the classical Fuller curve which for its optimal packing properties, is extensively used in concrete technology [24].

For a given cement content c, water-to-cement ratio w/c, specimen volume V, maximum aggregate size d_a, and minimum particle size d_0 (which governs the resolution of the model), particles to be placed inside the volume can be obtained as follows:

1. Compute aggregate volume fraction as $v_a = 1 - c/\rho_c - w/\rho_w - v_{air}$, where $w = (w/c)c$ is the water mass content per unit volume of concrete, $\rho_c = 3150\ \mathrm{kg/m^3}$ is the mass density

of cement, $\rho_w = 1000\ \mathrm{kg/m^3}$ is the mass density of water, and v_{air} is the volume fraction of entrapped or entrained air (typically 3–4%);

2. Compute the volume fraction of simulated aggregate as $v_{a0} = [1 - F(d_0)]v_a = [1 - (d_0/d_a)^{n_F}]v_a$;
3. Compute the total volume of simulated aggregate as $V_{a0} = v_{a0}V$;
4. Compute particle diameters by sampling the cdf in Eq. (2) by a random number generator: $d_i = d_0[1 - P_i(1 - d_0^q/d_a^q)]^{-1/q}$, where P_i is a sequence of random numbers between 0 and 1. Fig. 1a shows a graphical representation of the particle diameter selection procedure.
5. For each newly generated particle in the sequence, check that the total volume of generated particles $\widetilde{V}_{a0} = \sum_i \left(\pi d_i^3/6\right)$ does not exceed V_{a0}. When, for the first time, $\widetilde{V}_{a0} > V_{a0}$ occurs, the current generated particle is discarded, and the particle generation is stopped.

Fig. 1b shows the comparison between the theoretical sieve curve (solid line) and the computational sieve curve (circles), obtained through the procedure highlighted above for the generation of a 100-mm-side cube of concrete characterized by $c = 300\ \mathrm{kg/m^3}$, $w/c = 0.5$, $n_F = 0.5$, $d_0 = 4$ mm, and $d_a = 8$ mm.

In order to simulate the external surfaces of the specimen volume, the generated particles are augmented with zero-diameter particles (nodes). Assuming that the external surfaces of the specimen volume can be described through sets of vertexes, edges, and polyhedral faces, one node for each vertex is first added to the particle list. Then, $N_e = \mathrm{INT}(L_e/h_s)$ and $N_p = \mathrm{INT}\left(A_p/h_s^2\right)$ (where the operator $\mathrm{INT}(x)$ extracts the integer part of the argument x) nodes are associated with each edge e and polyhedral face p, respectively. L_e is the length of a generic surface edge, A_p is the area of a generic surface polyhedron, and the average surface mesh size h_s is chosen such that the resolution of the discretization on the surface is comparable to the one inside the specimen. Numerical experiments

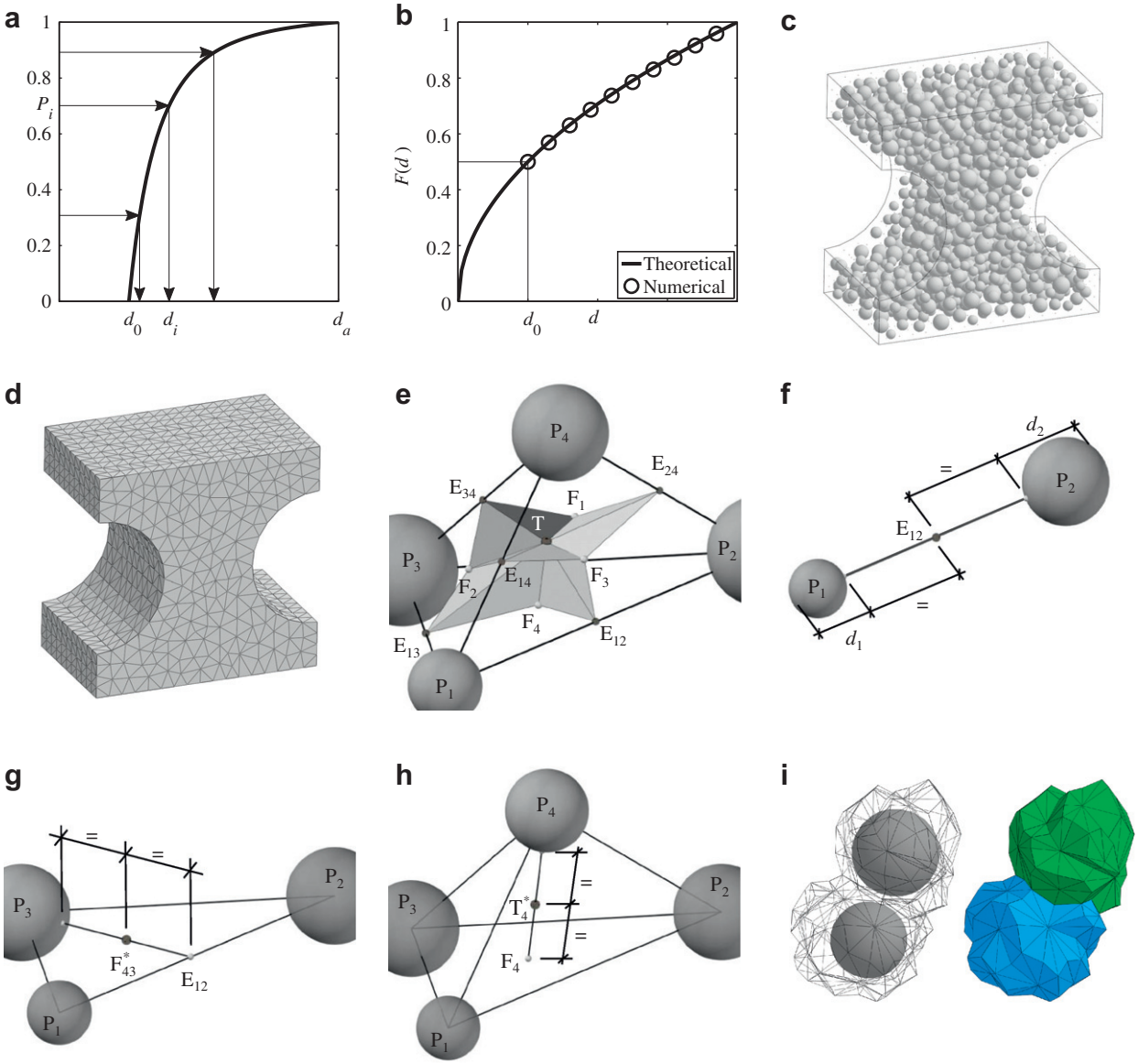

Fig. 1. (a) Probability distribution function for particle size generation; (b) theoretical (solid curve) and numerical (circles) sieve curve; (c) particle system for a typical dog-bone specimen; (d) tetrahedralization for a typical dog-bone specimen; (e) tessellation of a typical LDPM tetrahedron connecting four adjacent particles; (f) edge-point definition; (g) face-point definition; (h) tet-point definition; and (i) LDPM cells for two adjacent aggregate particle.

performed in this study show that this can be achieved by setting $h_s = \xi_s d_0$ with $\xi_s = 1.5$.

2.2. Definition of particle position

The second step of the geometrical characterization of concrete mesostructure is relevant to the random distribution of the generated particles on vertexes, edges, surface faces, and interior volume. First, the vertex nodes are placed. Secondly, nodes are distributed over the edges and surfaces by allowing a minimum distance of $\delta_s d_0$ to minimize the geometrical bias of the discretization. On the basis of several numerical simulations performed in this study, the value $\delta_s = 1.1$ seems to be appropriate to most situations. Finally, to generate a statistically isotropic random mesostructure, the centers of particles are placed throughout the volume of the specimen one by one (from the largest to the smallest) by using a procedure introduced in the concrete literature by Bažant [5] and also used by Cusatis et al. [16]. In this procedure, after generating a new particle position by a random number generator, a check is made for possible overlaps of this particle with previously placed particles and with the surface nodes. During this phase, the surface nodes are assigned a fictitious diameter of $\delta_s d_0$, and a minimum distance of $d_i/2 + d_j/2 + \zeta d_0$ between the centers of particles with diameters d_i and d_j is enforced. For $\zeta = 0$ or very small values of ζ, the particle distribution tends not to be statistically isotropic and presents zones of high particle density and zones with low particle density. On the contrary, for large values of ζ, the specimen volume becomes saturated quickly, and particle placement cannot be completed. Extensive numerical experiments conducted by the authors in this research show that $\zeta = 0.2$ avoids volume saturation in most cases while leading to relatively uniform particle distributions. Fig. 1c shows the particle system generated to simulate a dog-bone shaped specimen.

2.3. Definition of the lattice system

The third step of the construction of concrete mesostructure consists of defining the topology of the interaction among the particles. This is obtained by Delaunay tetrahedralization [21,2], which uses the nodal coordinates of the particle centers as input and gives a three-dimensional mesh of tetrahedra as output. These tetrahedra do not overlap, fill all the volume of the specimen, and have vertices coinciding with the given particle centers. In this study, the Delaunay tetrahedralization is performed by using TetGen [31]. TetGen implements a very robust algorithm for the computation of conforming (constrained) Delaunay triangulations and allows modeling of non-convex geometries such as specimens with notches and cutouts. Fig. 1d shows the Delaunay tetrahedralization of the dog-bone shaped specimen whose particle system is shown in Fig. 1c.

2.4. Definition of potential material failure locations

Finally, the fourth step for the characterization of concrete mesostructure deals with the definition of potential material failure locations at the meso-scale. As in previous work by Cusatis [16], it is assumed here that damage/fracture initiation and evolution occur in the cement paste (or fine mortar) between aggregate pieces, which remain mostly undamaged during the loading process.

In the previous works by Cusatis et al. [18,19], each edge of the Delaunay tetrahedra was interpreted as a connecting strut between two adjacent particles, and an effective area of the strut was defined by performing a tessellation of the domain anchored to the Delaunay tetrahedralization. This edge-based interaction is very effective and allows a good representation of concrete fracturing behavior as well as concrete failure under unconfined compression. However, since edge-based interaction involves only the kinematics of two particles; it does not provide an accurate description of volumetric effects that are important to correctly describe the compressive behavior of concrete under high confining pressure. As will be discussed in the next section, the mechanics of particle interaction in the present study are based on an analysis of an assemblage of four particles located at the vertices of a tetrahedron. Consequently, the definition of the surfaces through which interaction forces are exchanged between particles, which corresponds to damage localization zones, is based on the local geometry of each tetrahedron and the corresponding particles.

Since the tetrahedralization of the particle centers is constructed through the Delaunay algorithm, a straightforward tessellation would be the Voronoi tessellation. However, the Voronoi cells intersect the Delaunay edges at the mid-points of the edges. This feature is not appealing because, in the general case of unequal adjacent particles, the surface of the cells is likely to intersect the particles (aggregate pieces). More in general, the tessellation of a tetrahedron can be obtained by a set of triangles in which each triangle is formed by a point on a tetrahedron edge (edge-points, points E in Fig. 1e), a point on a tetrahedron face (face-points, points F in Fig. 1e), and a point inside the tetrahedron (tet-point, point T in Fig. 1e). Since a tetrahedron has six edges and each edge is shared by two faces, such a tessellation results in a set of twelve triangular facets.

The selection of edge-points, face-points, and tet-points is somewhat arbitrary, but numerical experiments conducted in this study show that the procedure outlined below tends to minimize the intersection between the tessellating surfaces and the particles. Such property makes the representation of meso-scale crack paths consistent with the assumption that fracture initiates and propagates in the cement paste and/or fine mortar.

With reference to a tetrahedron, (Fig. 1e) in which vertices are labeled as 1–4, each face is labeled through the label of the vertex opposite to that face, and each edge is labeled through the labels of vertices attached to it. Note that, in Fig. 1e as well as in Figs. 1f–h and 2a–c, the distance between the particles was fictitiously enlarged for illustration purposes. Actual particle systems, such as the one shown in Fig. 1c, generally feature inter-particles gaps significantly smaller than the diameters of typical particles.

1. Edge-points are defined at midway of the counterpart of the edges not belonging to the associated particles (see point E_{12} in Fig. 1f for the edge between particle P_1 and P_2).
2. Face-points are defined as follows. For each face of the tetrahedron, first three points (for example, F^*_{41}, F^*_{42}, and F^*_{43} for face 4) located on the straight lines connecting each face vertex to the edge-point located on the edge opposite to the particle under consideration are identified. Similarly to the edge-points, these points are located at midway of the line counterpart not belonging to the associated particles. In Fig. 1g, the point F^*_{43} associated with vertex P_3 and edge-point E_{12} is shown. Then, the face-point is selected as the centroid of these three points (see points F in Fig. 1e).
3. Similarly to face-points, the tet-point is defined as the centroid T of the points T^*_1, T^*_2, T^*_3, and T^*_4 identified on the straight lines connecting each vertex of the tetrahedron with the face-point on the face opposite to the vertex under consideration and located at midway of the line counterpart not belonging to the associated particle. In Fig. 1h, the point T^*_4 associated with vertex P_4 is shown.

Finally, by collecting all the facets associated with one particle, one obtains a polyhedral cell containing the particle (see Fig. 1i).

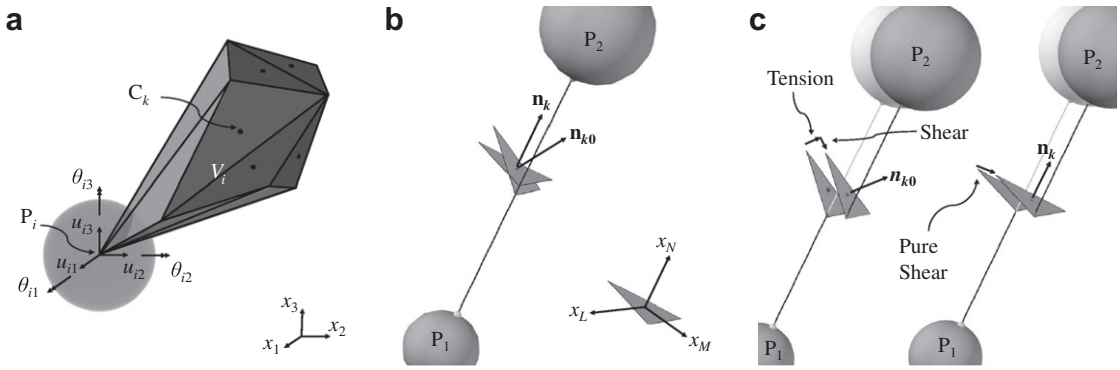

Fig. 2. (a) Portion of a tetrahedron associated to one particle; (b) original and projected LDPM facets; and (c) effect of meso-scale pure shear loading on one LDPM original facet (left) and one LDPM projected facet (right).

3. Discrete compatibility and equilibrium equations

The basic four-particle tetrahedron, depicted in Fig. 1h, is used here to derive the governing equations of the model. The tetrahedron is subdivided into four subdomains V_i ($i = 1,\ldots,4$), each defined by one node (particle), a portion of the three tetrahedron edges attached to the node, and the six triangular tessellation facets attached to the three edges (see Fig. 2a).

In each subdomain, the displacement field is defined through rigid-body kinematics. For $\mathbf{x} = [x_1,x_2,x_3]^T \in V_i$, one can write

$$\mathbf{u}(\mathbf{x}) = \mathbf{u}_i + \boldsymbol{\theta}_i \times (\mathbf{x} - \mathbf{x}_i) = \mathbf{A}_i(\mathbf{x})\mathbf{Q}_i \tag{4}$$

where

$$\mathbf{A}_i(\mathbf{x}) = \begin{bmatrix} 1 & 0 & 0 & 0 & x_3 - x_{3i} & x_{2i} - x_2 \\ 0 & 1 & 0 & x_{3i} - x_3 & 0 & x_1 - x_{1i} \\ 0 & 0 & 1 & x_2 - x_{2i} & x_{1i} - x_1 & 0 \end{bmatrix} \tag{5}$$

The vector $\mathbf{x}_i$ describes the position of node i, and the vector $\mathbf{Q}_i^T = [\mathbf{u}_i^T \boldsymbol{\theta}_i^T]$ collects the translational, $\mathbf{u}_i^T = [u_{1i}u_{2i}u_{3i}]$, and rotational, $\boldsymbol{\theta}_i^T = [\theta_{1i}\theta_{2i}\theta_{3i}]$, degrees of freedom of node i (see Fig. 2a).

By using Eq. (4), it is possible to define a displacement jump at the centroid C of each facet in the tetrahedron

$$[\![\mathbf{u}_{Ck}]\!] = \mathbf{u}_{Cj} - \mathbf{u}_{Ci} \tag{6}$$

where i and j are the nodes adjacent to facet k, and $\mathbf{u}_{Cj} = \mathbf{u}(\mathbf{x}_{Ck}^+)$ and $\mathbf{u}_{Ci} = \mathbf{u}(\mathbf{x}_{Ck}^-)$ are the displacements at the facet centroid C_k for $\mathbf{x}_{Ck}^- \in V_i, \mathbf{x}_{Ck}^+ \in V_j$ (see Table 1 for the permutation of indices i, j, and k).

By dividing the displacement jump by the edge length, it is possible to define a facet strain vector as $\ell_e^{-1}[\![\mathbf{u}_{Ck}]\!]$, where $\ell_e = \|\mathbf{x}_j - \mathbf{x}_i\| = [(\mathbf{x}_j - \mathbf{x}_i)^T(\mathbf{x}_j - \mathbf{x}_i)]^{1/2}$ is the length of edge e (Table 1). In order to formulate a constitutive law featuring the classical tension-compression asymmetry of concrete behavior, the strain vector $\ell_e^{-1}[\![\mathbf{u}_{Ck}]\!]$ needs to be decomposed into its normal and shear components. This is accomplished with reference to the projection of the tessellation facets into planes orthogonal to the edges (see Fig. 2b). The projected facets, as opposed as the original ones, are used for the definition of LDPM strain components to avoid non-symmetric behavior under pure shear. This issue is clarified in more detail in Fig. 2c in which the effect of a shear relative displacement between two particles, which is orthogonal to the edge, is analyzed. If the facet is not orthogonal to the edge (see Fig. 2c-left), the shear relative displacement can cause either tension or compression depending on its sign. Due to lack of symmetry of concrete behavior in tension and compression, this leads to sign-dependent meso-scale shear behavior that, in turn, causes stress locking during tensile fracturing simulations. Such a spurious effect disappears if one formulates the mechanical interaction between particles on the projection of the facets in a plane orthogonal to the edge (Fig. 2c-right).

Table 1
Facet, edge, and node indices.

Facet k	Edge e	Node i	Node j
1, 2	1	1	2
3, 4	2	1	3
5, 6	3	2	3
7, 8	4	2	4
9, 10	5	3	4
11, 12	6	1	4

The strains components can be then defined as

$$\varepsilon_{Nk} = \frac{\mathbf{n}_k^T[\![\mathbf{u}_{Ck}]\!]}{\ell_e} = \mathbf{B}_N^{jk}\mathbf{Q}_j - \mathbf{B}_N^{ik}\mathbf{Q}_i \tag{7}$$

$$\varepsilon_{Mk} = \frac{\mathbf{m}_k^T[\![\mathbf{u}_{Ck}]\!]}{\ell_e} = \mathbf{B}_M^{jk}\mathbf{Q}_j - \mathbf{B}_M^{ik}\mathbf{Q}_i \tag{8}$$

$$\varepsilon_{Lk} = \frac{\mathbf{l}_k^T[\![\mathbf{u}_{Ck}]\!]}{\ell_e} = \mathbf{B}_L^{jk}\mathbf{Q}_j - \mathbf{B}_L^{ik}\mathbf{Q}_i \tag{9}$$

where $\mathbf{n}_k = (\mathbf{x}_j - \mathbf{x}_i)/\ell_e$, $\mathbf{m}_k$, and $\mathbf{l}_k$ are two mutually orthogonal directions in the plane of the projected facets, $\mathbf{B}_N^{pk} = (1/\ell_e)\mathbf{n}_k^T\mathbf{A}_p(\mathbf{x}_{Ck})$, $\mathbf{B}_M^{pk} = (1/\ell_e)\mathbf{m}_k^T\mathbf{A}_p(\mathbf{x}_{Ck})$, and $\mathbf{B}_L^{pk} = (1/\ell_e)\mathbf{l}_k^T\mathbf{A}_p(\mathbf{x}_{Ck}), p = i,j$. Eqs. (7)–(9) represent the discrete compatibility equations of the LDPM formulation.

The meso-scale constitutive law, described in the next Section, allows the calculation of the normal and shear stresses at each facet. Formally, one can write $\boldsymbol{\sigma}_k = \mathbf{F}(\boldsymbol{\varepsilon}_k, \xi_k)$, where $\boldsymbol{\sigma}_k$, $\boldsymbol{\varepsilon}_k$, and ξ_k are vectors collecting facet stresses, strains, and internal variables, respectively.

Finally, the governing equations can be completed by imposing the equilibrium through the Principle of Virtual Work (PVW). The internal work associated with a generic facet can be expressed as

$$\delta\mathscr{W}_k = \ell_e A_k \boldsymbol{\sigma}_k^T \delta\boldsymbol{\varepsilon}_k = \ell_e A_k(\sigma_{Nk}\delta\varepsilon_{Nk} + \sigma_{Mk}\delta\varepsilon_{Mk} + \sigma_{Lk}\delta\varepsilon_{Lk}) \tag{10}$$

where A_k is the projected facet area.

By substituting Eqs. (7)–(9) into Eq. (10), one obtains

$$\delta\mathscr{W}_k = \mathbf{F}_{ik}^T\delta\mathbf{Q}_i + \mathbf{F}_{jk}^T\delta\mathbf{Q}_j \tag{11}$$

$$\mathbf{F}_{ik}^T = -\ell_e A_k(\sigma_{Nk}\mathbf{B}_N^{ik} + \sigma_{Mk}\mathbf{B}_M^{ik} + \sigma_{Lk}\mathbf{B}_L^{ik}) \tag{12}$$

$$\mathbf{F}_{jk}^T = \ell_e A_k(\sigma_{Nk}\mathbf{B}_N^{kj} + \sigma_{Mk}\mathbf{B}_M^{kj} + \sigma_{Lk}\mathbf{B}_L^{kj}) \tag{13}$$

that represent the nodal forces at node i and j associated with facet k. By summing up the contributions of all the facets and equating the total internal work with the total external work, one can obtain

the discrete equilibrium equations of the LDPM formulation. It can be shown that the equilibrium equations obtained through the PVW correspond exactly to the translational and rotational equilibrium of each polyhedral LDPM cell.

4. LDPM constitutive law

In this section, the LDPM constitutive law, which provides the relationship between the strain vector and the stress vector at the facet level, is presented. Hereinafter, the subscript k indicating the generic facet is dropped for sake of simplicity and readability of the equations.

4.1. Elastic behavior

The elastic behavior is formulated by assuming that normal and shear stresses are proportional to the corresponding strains:

$$\sigma_N = E_N \varepsilon_N; \sigma_M = E_T \varepsilon_M; \sigma_L = E_T \varepsilon_L \tag{14}$$

where $E_N = E_0$, $E_T = \alpha E_0$, E_0 = effective normal modulus, and α = shear-normal coupling parameter. E_0 and α are assumed to be material properties that can be identified from results of experimental tests in the elastic regime.

At the macroscopic level, concrete elastic behavior is statistically homogeneous and isotropic. As such, it can be modeled effectively through the classical theory of elasticity characterized by Young's modulus, E, and Poisson's ratio, v. The relationship between the meso-scale LDPM parameters, α and E_0, and the macroscopic elastic parameters, E and v, can be obtained by considering a limiting case in which an infinite number of facets surrounds one aggregate piece. In this case, the LDPM formulation corresponds to the kinematically constrained formulation of the microplane model without deviatoric/volumetric split of the normal strain component [14]. One can write

$$E_0 = \frac{1}{1-2v} E \Longleftrightarrow E = \frac{2+3\alpha}{4+\alpha} E_0 \tag{15}$$

and

$$\alpha = \frac{1-4v}{1+v} \Longleftrightarrow v = \frac{1-\alpha}{4+\alpha} \tag{16}$$

Figs. 3a and 3b compare the estimates according to Eqs. (15) and (16) (solid lines) to the macroscopic average Poisson's ratio and Young's modulus obtained numerically through LDPM simulations (circles). The LDPM simulations were performed on cubic 100-mm-side specimens generated with the following parameters: $w/c = 0.5$, $a/c = 6.5$, $c = 300\ \mathrm{Kg/m^3}$, $d_a = 8$ mm, $d_0 = 4$ mm, and $n_F = 0.5$. The LDPM data points (circles) were obtained by setting E_0 and α to given values and subjecting the specimens to end displacements corresponding to a macroscopic (average) strain of $E_{33} = 2 \times 10^{-4}$. The results of the simulations were post-processed to obtain the macroscopic (average) stress Σ_{33} and the macroscopic (average) transverse strains E_{11} and E_{22} from which the macroscopic Poisson's ratio and macroscopic Young's modulus were computed as $E = \Sigma_{33}/E_{33}$ and $v = -0.5(E_{11} + E_{22})/E_{33}$. The excellent agreement between the numerical and the analytical results suggests that Eqs. (15) and (16) can be used confidently to estimate the LDPM elastic parameters from macroscopic experimental measurements of Young's modulus and Poisson's ratio.

As it was pointed out by Bažant [6], Eq. (16) do not cover the entire range of thermodynamically acceptable Poisson's ratios (−1–0.5) since negative values of α (and consequently negative values of the shear stiffness) are associated with $v > 0.25$. Although this limitation may hamper the applicability of the LDPM framework to materials with $v > 0.25$, it does not affect the modeling of concrete for which Poisson's ratio is always about 0.2 or less. In the microplane formulation, the full Poisson's ratio range can be obtained by introducing the volumetric/deviatoric decomposition [14] of the normal component, $\varepsilon_N = \varepsilon_V + \varepsilon_D$, and by expressing normal and shear stresses as $\sigma_N = E_V\ \varepsilon_V + E_D \varepsilon_D$, $\sigma_M = E_D \varepsilon_M$, $\sigma_L = E_D \varepsilon_L$, where $E_V = E/(1-2v)$ and $E_D = E/(1+v)$ are the volumetric and deviatoric moduli, respectively. The same approach could be used for LDPM-type formulation; however in this way, the LDPM capability of correctly simulating splitting failure under compression (this being one of the unique features of LDPM) would be completely lost.

This point can be discussed in more detail considering Fig. 3c, in which a schematic representation of the stress path obtained by loading in compression a heterogeneous material is shown. Heterogeneities induce a deviation of the compressive stress path leading to the formation of transverse tensile stresses that, ultimately cause splitting failure. In the LDPM formulation in which the normal stress is proportional to the normal strain, the transverse tension is automatically captured. On the contrary, if the deviatoric-volumetric split is used, LDPM-type formulations reproduce the elastic solution of classical elasticity for homogeneous and isotropic materials. In this case, the stress path is undisturbed from the top to the bottom of the specimen, and no tensile stresses can be observed. In this situation, tensile failure is obviously not possible, and splitting cracks cannot initiate and propagate.

4.2. Inelastic behavior

The LDPM formulation of the nonlinear and inelastic behavior aims at representing three separate physical mechanisms characterizing meso-scale failure behavior: (1) fracturing and cohesive

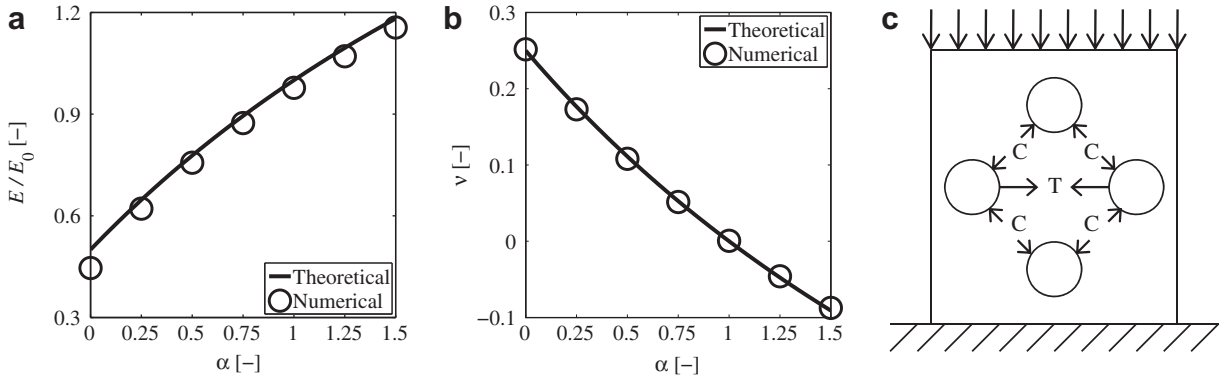

Fig. 3. (a) Relationship between macroscopic Young's modulus and LDPM elastic parameters ([-] means that the correspondent quantity is adimensional); (b) relationship between macroscopic Poisson's ratio and LDPM coupling parameter; and (c) idealization of the effect of compression on heterogeneous materials.

behavior under tension and tension/shear; (2) pore collapse and material compaction under high compressive stresses; and (3) frictional behavior.

4.2.1. Fracturing behavior

Fracturing behavior is characterized by tensile normal strains ($\varepsilon_N > 0$). As previously shown by Cusatis [16], it is convenient to formulate fracture and damage evolution by a relationship between the *effective strain*, ε, and the *effective stress*, σ, defined as

$$\varepsilon = \sqrt{\varepsilon_N^2 + \alpha(\varepsilon_M^2 + \varepsilon_L^2)}; \qquad \sigma = \sqrt{\sigma_N^2 + (\sigma_M^2 + \sigma_L^2)/\alpha} \tag{17}$$

By using the effective strain and the effective stress, the relationship between normal and shear stresses versus normal and shear strains can be formulated through damage-type constitutive equations (see derivation by Cusatis et al. [16]):

$$\sigma_N = \sigma\frac{\varepsilon_N}{\varepsilon}; \sigma_M = \sigma\frac{\alpha\varepsilon_M}{\varepsilon}; \qquad \sigma_L = \sigma\frac{\alpha\varepsilon_L}{\varepsilon} \tag{18}$$

The effective stress σ is assumed to be incrementally elastic, $\dot{\sigma} = E_0\dot{\varepsilon}$, and it is formulated such that it satisfies the inequality $0 \leqslant \sigma \leqslant \sigma_{bt}(\varepsilon,\omega)$, in which $\sigma_{bt}(\varepsilon,\omega)$ is a limiting boundary enforced through a vertical (at constant strain) return algorithm.

Following [16], the strain-dependent boundary $\sigma_{bt}(\varepsilon,\omega)$ can be expressed as

$$\sigma_{bt}(\varepsilon,\omega) = \sigma_0(\omega)\exp\left[-H_0(\omega)\frac{\langle\varepsilon_{\max} - \varepsilon_0(\omega)\rangle}{\sigma_0(\omega)}\right] \tag{19}$$

in which the brackets $\langle\cdot\rangle$ are used in Macaulay sense: $\langle x\rangle = \max\{x,0\}$.

The coupling variable ω represents the degree of interaction between shear and normal loading and is defined as [16]

$$\tan\omega = \frac{\varepsilon_N}{\sqrt{\alpha}\varepsilon_T} = \frac{\sigma_N\sqrt{\alpha}}{\sigma_T} \tag{20}$$

where $\varepsilon_T = \sqrt{\varepsilon_M^2 + \varepsilon_L^2}$ is the total shear strain, and $\sigma_T = \sqrt{\sigma_M^2 + \sigma_L^2}$ is the total shear stress. The boundary σ_{bt} evolves exponentially as a function of the maximum effective strain, which is a history-dependent variable defined as $\varepsilon_{\max} = \sqrt{\varepsilon_{N,\max}^2 + \alpha\varepsilon_{T,\max}^2}$, where $\varepsilon_{N,\max}(t) = \max_{\tau<t}[\varepsilon_N(\tau)]$ and $\varepsilon_{T,\max}(t) = \max_{\tau<t}[\varepsilon_T(\tau)]$ are the maximum normal and total shear strains, respectively, attained during the loading history. It is worth noting that in absence of unloading the maximum effective strain corresponds to the current value of the effective strain: $\varepsilon_{\max} \equiv \varepsilon$.

The function $\sigma_0(\omega)$ is the strength limit for the effective stress and is defined as

$$\sigma_0(\omega) = \sigma_t\frac{-\sin(\omega) + \sqrt{\sin^2(\omega) + 4\alpha\cos^2(\omega)/r_{st}^2}}{2\alpha\cos^2(\omega)/r_{st}^2} \tag{21}$$

in which $r_{st} = \sigma_s/\sigma_t$ is the ratio between the shear strength (cohesion), σ_s, and the tensile strength, σ_t. In the stress space $\sigma_N - \sigma_T$, Eq. (21) is a parabola with its axis of symmetry coinciding with the σ_N-axis (solid curve in Fig. 4a).

The exponential decay of the boundary σ_{bt} starts when the maximum effective strain reaches its elastic limit $\varepsilon_0(\omega) = \sigma_0(\omega)/E_0$, and the decay rate is governed by the post-peak slope (softening modulus), which is assumed to be a power function of the internal variable ω:

$$H_0(\omega) = H_t\left(\frac{2\omega}{\pi}\right)^{n_t} \tag{22}$$

Eq. (22) provides a smooth transition from softening behavior under pure tensile stress, $H_0(\pi/2) = H_t$, to perfectly plastic behavior under pure shear, $H_0(0) = 0$. In order to preserve the correct energy dissipation during meso-scale damage localization [4], the softening modulus in pure tension is expressed as $H_t = 2E_0/(\ell_t/\ell - 1)$, where $\ell_t = 2E_0G_t/\sigma_t^2$, G_t is the meso-scale fracture energy, and ℓ is the length of the tetrahedron edge associated with the current facet.

The dashed curve in Fig. 4a represents the strength domain (computed from the boundary σ_{bt}) corresponding to $\varepsilon_{\max} = 4\sigma_t/E_0$. As one can see, as damage progresses, the strength domain shrinks and tends to become concave. This characteristic is important in order to correctly simulate the different ductilities in tension and compression at the macro-scale. It is also worth noting that, in damage mechanics (contrary to plasticity), the lack of convexity of the strength domain does not violate thermodynamics restrictions on the energy dissipation, and as such, it is a completely acceptable feature of the formulation.

Fig. 4b shows the normal and shear stress versus strain relationships for $\omega = 0$ (pure shear), $\omega = \pi/2$ (pure tension), and $\omega = \pi/8$. The plots were generated by setting, for illustration purposes, $\ell = 10$ mm, $\alpha = 0.25$, $E_0 = 30{,}000$ MPa, $\sigma_t = 3$ MPa, $\sigma_s = 4.5$ MPa, $\ell_t = 100$ mm, and $n_t = 0.2$.

Finally, the fracturing formulation needs to be completed by unloading-reloading rules to simulate cycling loadings. Fig. 4c illustrates the unloading-reloading rule adopted in this work in terms of effective stress versus effective strain relationship. Let's assume that unloading occurs after the effective strain increased continuously from zero to a certain value $\varepsilon_{\max}$. The effective stress decreases elastically until it reaches a zero value and remains constant at zero for further decreases of the effective strain. During reloading, the effective stress remains zero until the effective strain reaches the reloading strain limit, ε_{tr}, and, beyond this point, the behavior is incrementally elastic. The reloading strain limit is defined as $\varepsilon_{tr} = k_t(\varepsilon_{\max} - \sigma_{bt}/E_0)$, where k_t is assumed to be a material parameter. The parameter k_t governs the size of hysteresis cycles and, consequently, the amount of energy that the material can dissipate during cycling loading. For $k_t = 1$, the dissipated energy is zero, whereas for $k_t = 0$, it is a maximum and equal to $A\ell\sigma_{bt}\varepsilon_{\max}$ for a given $\varepsilon_{\max}$ on a facet of projected area A and associated with a lattice edge length ℓ.

4.2.2. Pore collapse and material compaction

Under high compressive hydrostatic deformations, concrete behavior exhibits strain-hardening plasticity. The plastic behavior is characterized by an initial phase in which micro-scale and meso-scale pores collapse under load, and a later phase, in which the walls of completely collapsed pores are in contact leading to a significant densification of the material [25]. In terms of stress-strain response, the first phase is associated with a sudden decrease of the stiffness that is later regained in the second phase (rehardening). Experiments show [3] that after the densification phase, both the tangent plastic stiffness and the unloading elastic stiffness are, in some cases, even larger than the initial elastic stiffness. Finally, rehardening is limited (or even negligible) in the presence of significant deviatoric deformations, which typically leads to a horizontal plateau in the measured macroscopic stress versus strain curves.

LDPM constitutive law simulates the phenomena discussed above through a strain-dependent normal boundary limiting the compressive normal stress component at the facet level. This compressive boundary, $\sigma_{bc}(\varepsilon_D,\varepsilon_V)$, is assumed to be a function of the volumetric strain ε_V and the deviatoric strain ε_D. The volumetric strain is computed at the tetrahedron level as $\varepsilon_V = (V - V_0)/V_0$, where V and V_0 are the current and initial volume of the tetrahedron, respectively. The current volume is computed by neglecting the effect of nodal rotations. A more rigorous definition of volumetric strain in the framework of discrete models and accounting for particle rotations is provided by Cusatis and Schauffert [20]. In each LDPM tetrahedron, all twelve facets are assumed to be subject to the same volumetric strain, whereas each facet is characterized

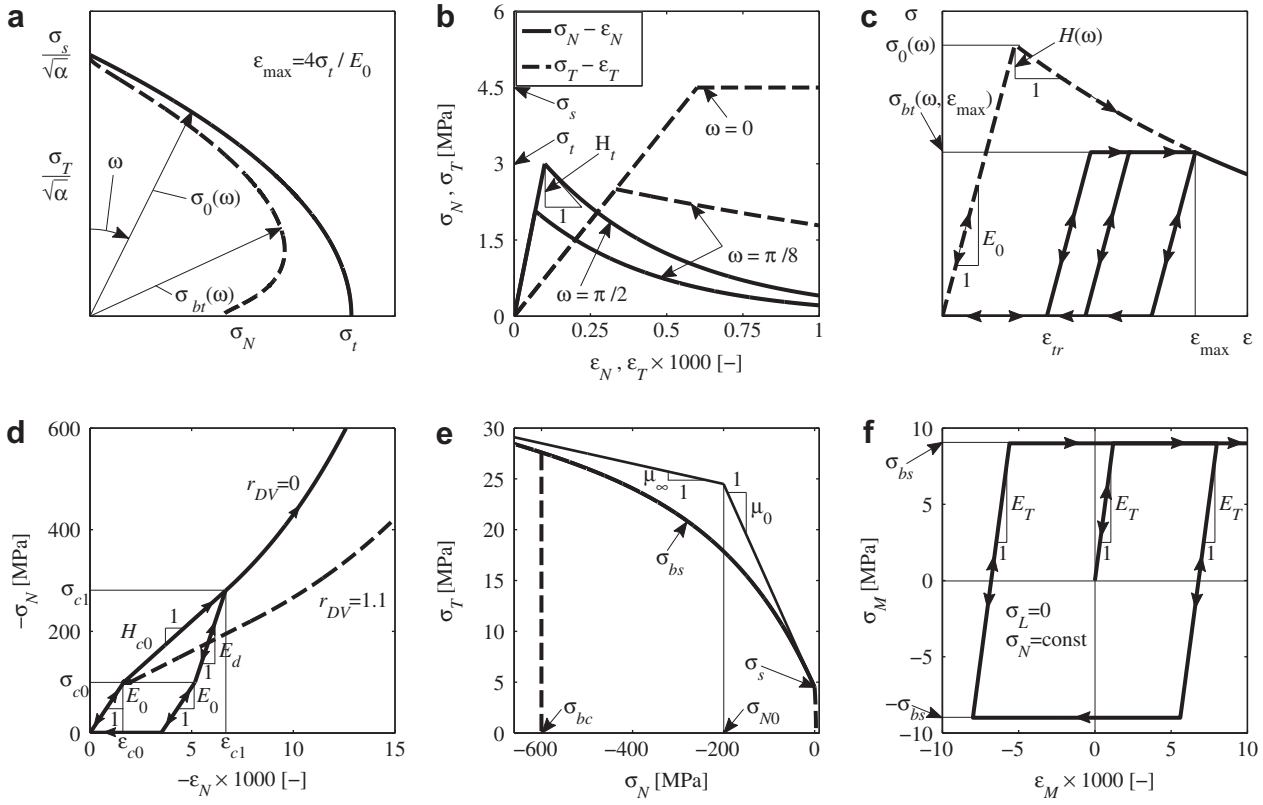

Fig. 4. LDPM constitutive laws. (a) Virgin and damaged shear strength as function of positive normal stresses; (b) Typical stress versus strain curves at the LDPM facet level; (c) Unloading-reloading model; (d) Typical normal stress versus normal strain curves in compression; (e) Shear strength as a function of negative normal stresses (frictional behavior); and (f) Typical shear stress versus shear strain curve.

by a different value of the deviatoric strain calculated by subtracting the volumetric strain from the normal strain: $\varepsilon_D = \varepsilon_N - \varepsilon_V$. The definition of the volumetric and deviatoric strains are completely equivalent to the same quantities defined at each microplane in the microplane model formulation [6].

For a constant deviatoric-to-volumetric strain ratio, $r_{DV} = \varepsilon_D/\varepsilon_V$, the compressive boundary is assumed to have an initial linear evolution (modeling pore collapse and yielding) followed by an exponential evolution (modeling compaction and rehardening). One can write

$$\sigma_{bc}(\varepsilon_D, \varepsilon_V) = \begin{cases} \sigma_{c0} & \text{for } -\varepsilon_{DV} \leqslant 0 \\ \sigma_{c0} + \langle -\varepsilon_{DV} - \varepsilon_{c0} \rangle H_c(r_{DV}) & \text{for } 0 \leqslant -\varepsilon_{DV} \leqslant \varepsilon_{c1} \\ \sigma_{c1}(r_{DV}) \exp[(-\varepsilon_{DV} - \varepsilon_{c1}) H_c(r_{DV})/\sigma_{c1}(r_{DV})] & \text{otherwise} \end{cases} \tag{23}$$

where $\varepsilon_{DV} = \varepsilon_V + \beta\varepsilon_D$ (compaction strain), β is a material parameter, σ_{c0} is the meso-scale yielding compressive stress, $\varepsilon_{c0} = \sigma_{c0}/E_0$ is the compaction strain at the onset of pore collapse, $H_c(r_{DV})$ is the initial hardening modulus, $\varepsilon_{c1} = \kappa_{c0}\varepsilon_{c0}$ is the compaction strain at which rehardening begins, κ_{c0} is the material parameter governing the onset of rehardening, and $\sigma_{c1}(r_{DV}) = \sigma_{c0} + (\varepsilon_{c1} - \varepsilon_{c0})H_c(r_{DV})$. The compaction strain ε_{DV} corresponds to the volumetric strain for $\beta = 0$ and to the normal strain for $\beta = 1$; it controls the extent of volumetric effects on the meso-scale compressive behavior and influences the macroscopic triaxial response in compression. In this study the value $\beta = 0$ will be assumed.

For increasing r_{DV}, the slope of the initial hardening modulus needs to tend to zero in order to simulate the observed horizontal plateau featured by typical experimental data. This can be achieved by setting

$$H_c(r_{DV}) = \frac{H_{c0}}{1 + \kappa_{c2}\langle r_{DV} - \kappa_{c1} \rangle} \tag{24}$$

where H_{c0}, κ_{c1}, and κ_{c2} are assumed to be material parameters.

For compressive loading ($\varepsilon_N < 0$), the normal stress is computed by imposing the inequality $-\sigma_{bc}(\varepsilon_D, \varepsilon_V) \leqslant \sigma_N \leqslant 0$. Within the boundaries of this inequality, the behavior is assumed to be incrementally elastic: $\dot{\sigma}_N = E_{Nc}\dot{\varepsilon}_N$. In order to model the increased stiffness during unloading, the loading-unloading stiffness E_{Nc} is defined as

$$E_{Nc} = \begin{cases} E_0 & \text{for} -\sigma_N < \sigma_{c0} \\ E_d & \text{otherwise} \end{cases} \tag{25}$$

where E_d is the densified normal modulus. For loading processes at constant r_{DV}, we have and $\varepsilon_{DV} = \varepsilon_V(1 + \beta r_{DV}) = \varepsilon_N(1 + \beta\ r_{DV})/(1 + r_{DV})$. In this case, the boundary in Eq. (23) can be expressed as a function of the normal strain ε_N, shown in Fig. 4d, where the solid and dashed curves represent, respectively, the compressive normal stress versus strain relationship for $r_{DV} = 0$ and $r_{DV} = 1.1$. For the case of $r_{DV} = 0$, the unloading-reloading rule is also shown. For illustration purposes, we assumed parameter values of $E_0 = 60{,}000$ MPa, $\sigma_{c0} = 100$ MPa, $H_{c0}/E_0 = 0.6$, $\kappa_{c0} = \varepsilon_{c1}/\varepsilon_{c0} = 4$, $E_d/E_0 = 2$, $\kappa_{c1} = 1$, and $\kappa_{c2} = 5$. It is worth noting that the curve relevant to $r_{DV} = 0$ tend, to a straight line with slope equal to E_d for strains such that the slope of the compressive boundary in Eq. (23) is higher than E_d.

4.2.3. Frictional behavior

Finally, in the presence of compressive stresses, the shear strength increases due to frictional effects. As often done in the literature, frictional phenomena can be simulated effectively through classical incremental plasticity [22]. Incremental shear stresses can be calculated as $\dot{\sigma}_M = E_T(\dot{\varepsilon}_M - \dot{\varepsilon}_M^p)$ and $\dot{\sigma}_L = E_T(\dot{\varepsilon}_L - \dot{\varepsilon}_L^p)$, where the

plastic strain increments are assumed to obey the normality rule $\dot{\varepsilon}_M^p = \dot{\lambda}\partial\varphi/\partial\sigma_M$ and $\dot{\varepsilon}_L^p = \dot{\lambda}\partial\varphi/\partial\sigma_L$.

The plastic potential can be expressed as $\varphi = \sqrt{\sigma_M^2 + \sigma_L^2} - \sigma_{bs}(\sigma_N)$ in which the shear strength σ_{bs} is formulated with a nonlinear frictional law:

$$\sigma_{bs}(\sigma_N) = \sigma_s + (\mu_0 - \mu_\infty)\sigma_{N0} - \mu_\infty\sigma_N - (\mu_0 - \mu_\infty)\sigma_{N0} \times \exp(\sigma_N/\sigma_{N0}) \tag{26}$$

where σ_s is the cohesion (previously introduced in this paper), μ_0 and μ_∞ are the initial and final internal friction coefficients, respectively, and σ_{N0} is the normal stress at which the internal friction coefficient transitions from μ_0 to μ_∞. As shown in Fig. 4e, the frictional law in Eq. (26) tends to the asymptote $\sigma_s + (\mu_0 - \mu_\infty)\sigma_{N0} - \mu_\infty\sigma_N$ characterized by a slope equal to μ_∞ and whose intercept with the σ_T-axis increases with increasing σ_{N0}. The parameter σ_{N0} basically governs the extent of the nonlinearity of the shear boundary. The classical linear (Coulomb-type) frictional law with slope μ_0 or μ_∞ is obtained by setting $\sigma_{N0} = \infty$ or $\sigma_{N0} = 0$, respectively. Finally, equations governing the shear stress evolution must be completed by the loading-unloading conditions, which can be expressed through the classical Kuhn–Tucker's conditions: $\varphi\dot{\lambda} \leqslant 0$ and $\dot{\lambda} \geqslant 0$. Typical shear versus strain relationship is shown in Fig. 4f.

5. Numerical implementation and stability analysis

The LDPM computational framework formulated in this paper was implemented into the MARS code [28], which is a multi-purpose structural analysis program based on a modern object-oriented architecture. MARS performs structural analysis by an explicit dynamic algorithm (based on a central difference scheme) and is very effective in the management of the various computational entities (nodes, finite elements, loads, etc.) making possible the numerical simulation of very large systems even on regular desktop computers. These features are particularly attractive for the research presented in this paper since LDPM calculations often involve several thousands of degrees of freedom. In addition, the explicit character of the computational scheme implemented in MARS makes it advantageous because is not affected by the convergence problems that implicit schemes often have in handling softening behavior.

Explicit algorithms, however, are not unconditionally stable and require an accurate evaluation of the numerical stability of the numerical simulations. In the elastic regime, the stability condition can be expressed as $\Delta t < 2/\omega_{\max}$, where $\omega_{\max}$ represents the highest natural frequency of the computational system. It can be shown [8] that $\omega_{\max} < \max(\omega_I)$, where ω_I are the natural frequencies of the individual unrestrained elements composing the mesh used in the simulation. Based on this observation, the stable time step for the LDPM can be estimated by computing the natural frequencies of each LDPM tetrahedra. This requires solving the eigenvalue problem $\det(\mathbf{K} - \omega^2\mathbf{M}) = 0$, where $\mathbf{K}$ is the stiffness matrix and $\mathbf{M}$ is the mass matrix.

The elastic energy associated with a generic facet k is

$$\mathscr{U}_k = \frac{1}{2}\ell_e A_k\left(E_N\varepsilon_{Nk}^2 + E_T\varepsilon_{Lk}^2 + E_T\varepsilon_{Mk}^2\right) = \frac{1}{2}\left[\mathbf{Q}_j^{\mathrm{T}}\left(\mathbf{K}_{ij}^k + \mathbf{K}_{jj}^k\right)\mathbf{Q}_j + \mathbf{Q}_i^{\mathrm{T}}\left(\mathbf{K}_{ii}^k + \mathbf{K}_{ji}^k\right)\mathbf{Q}_i\right] \tag{27}$$

where $\mathbf{K}_{pq}^k = E_N\left(\mathbf{B}_N^{pk}\right)^{\mathrm{T}}\mathbf{B}_N^{qk} + E_T\left(\mathbf{B}_M^{pk}\right)^{\mathrm{T}}\mathbf{B}_M^{qk} + E_T\left(\mathbf{B}_L^{pk}\right)^{\mathrm{T}}\mathbf{B}_L^{qk}(p,q = i,j)$.

The overall tetrahedron stiffness matrix is obtained by assembling the stiffness contributions of all twelve facets:

$$\mathbf{K} = \sum_{k=1}^{12}\mathbf{K}^k = \sum_{k=1}^{12}\begin{bmatrix}\mathbf{K}_{ii}^k & \mathbf{K}_{ij}^k \\ \mathbf{K}_{ji}^k & \mathbf{K}_{jj}^k\end{bmatrix} \tag{28}$$

where the symbol $\sum$ is used to identify the assemblage operation. The kinetic energy associated with a generic facet k can be subdivided into two terms associated with the two nodes (i and j, see Table 1) adjacent to the facet: $\mathscr{T}_k = \mathscr{T}_{ki} + \mathscr{T}_{kj}$. Each individual term reads

$$\mathscr{T}_{kp} = \frac{1}{2}\int_{V_{kp}}\rho\dot{\mathbf{u}}(\mathbf{x})^{\mathrm{T}}\dot{\mathbf{u}}(\mathbf{x})dV = \frac{1}{2}\dot{\mathbf{Q}}_p^{\mathrm{T}}\left[\int_{V_{kp}}\rho\mathbf{A}_p(\mathbf{x})^{\mathrm{T}}\mathbf{A}_p(\mathbf{x})dV\right]\dot{\mathbf{Q}}_p = \frac{1}{2}\dot{\mathbf{Q}}_p^{\mathrm{T}}\mathbf{M}_p^k\dot{\mathbf{Q}}_p \tag{29}$$

where

$$\mathbf{M}_p^k = \rho\begin{bmatrix} V_{kp} & 0 & 0 & 0 & \mathscr{S}_{kp}^z & -\mathscr{S}_{kp}^y \\ 0 & V_{kp} & 0 & -\mathscr{S}_{kp}^z & 0 & \mathscr{S}_{kp}^x \\ 0 & 0 & V_{kp} & \mathscr{S}_{kp}^y & -\mathscr{S}_{kp}^x & 0 \\ 0 & -\mathscr{S}_{kp}^z & \mathscr{S}_{kp}^y & \mathscr{I}_{kp}^y + \mathscr{I}_{kp}^z & -\mathscr{I}_{kp}^{xy} & -\mathscr{I}_{kp}^{xz} \\ \mathscr{S}_{kp}^z & 0 & -\mathscr{S}_{kp}^x & -\mathscr{I}_{kp}^{xy} & \mathscr{I}_{kp}^x + \mathscr{I}_{kp}^z & -\mathscr{I}_p^{yz} \\ -\mathscr{S}_{kp}^y & \mathscr{S}_{kp}^x & 0 & -\mathscr{I}_{kp}^{xz} & -\mathscr{I}_{kp}^{yz} & \mathscr{I}_{kp}^x + \mathscr{I}_{kp}^y \end{bmatrix} \tag{30}$$

and $\rho = c(w/c + a/c) + \rho_{air}v_{air}$ is material density, ρ_{air} is 1.2 Kg/m^3 (at sea level and at 15°C), and V_{kp} is the volume identified by the facet k and the node p. The various terms appearing in the matrix $\mathbf{M}_p^k$ are first order (symbols $\mathscr{S}$) and second order (symbols $\mathscr{I}$) moments of the volume V_{kp} about the axes of a cartesian system of reference with origin at node p.

Similar to the stiffness matrix, the overall tetrahedron mass matrix is obtained by assembling the contributions of the twelve facets

$$\mathbf{M} = \sum_{k=1}^{12}\mathbf{M}^k = \sum_{k=1}^{12}\begin{bmatrix}\mathbf{M}_i^k & \mathbf{0} \\ \mathbf{0} & \mathbf{M}_j^k\end{bmatrix} \tag{31}$$

The mass matrix in Eq. (31) is, in general, not diagonal. In order to take full advantage of the explicit algorithm used in this study, a diagonalized version of $\mathbf{M}$ is obtained by simply discarding the non-diagonal terms. It is worth noting that by using the diagonalized matrix, the mass term of a certain particle node is exact if the particle node is the mass centroid of the LDPM cell. This is approximately the case for many particle nodes in the interior of typical LDPM systems.

6. Concluding remark

The Lattice Discrete Particle Model (LDPM) formulated in this paper has several unique features and potential capabilities, which, however, need to be verified by performing numerical simulations and comparing numerical results with experimental data. Part II of this study, which follows, presents an extensive calibration and validation of LDPM.

Acknowledgment

This effort was sponsored by the US Army Engineer Research and Development Center. Permission to publish was granted by the Director, Geotechnical and Structures Laboratory. The work of first author was also supported under NSF grant No 0928448 and DTRA grant No HDTRA1-09-1-0029 to Rensselaer Polytechnic Institute.

References

[1] Arslan A, Ince R, Karihaloo BL. Improved lattice model for concrete fracture. J Eng Mech – ASCE 2002;128(1):57–65.

[2] Barber CB, Dopkin DP, Huhdanpaa HT. The quickhull algorithm for convex hulls. ACM Trans Math Softw 1996;22(4):469–83.
[3] Bazant ZP, Bishop FC, Chang TP. Confined compression tests of cement paste and concrete up to 300-ksi. J Am Conc Inst 1986;83(4):553–60.
[4] Bazant ZP, Oh B-H. Crack band theory for fracture of concrete. Mater Struct (RILEM, Paris) 1983;16:155–77.
[5] Bazant ZP, Tabbara MR, Kazemi MT, Pijaudier Cabot G. Random particle model for fracture of aggregate or fiber composites. J Eng Mech – ASCE 1990;116(8):1686–705.
[6] Bazant ZP, Xiang YY, Prat PC. Microplane model for concrete. I. Stress-strain boundaries and finite strain. J Eng Mech – ASCE 1996;122(3):245–54.
[7] Belheine N, Plassiard JP, Donzé FV, Darve F, Seridi A. Numerical simulation of drained triaxial test using 3d discrete element modeling. Comput Geotech 2009;36(1-2):320–31.
[8] Belytschko T, Liu WK, Moran B. Nonlinear finite elements for continua and structures. Chichester, England: WILEY; 2000.
[9] Bolander JE, Saito S. Fracture analyses using spring networks with random geometry. Eng Fract Mech 1998;61(5-6):569–91.
[10] Bolander JE, Shiraishi T, Isogawa Y. An adaptive procedure for fracture simulation in extensive lattice networks. Eng Fract Mech 1996;54(3):325–34.
[11] Caballero A, Carol I, Lopez CM. A meso-level approach to the 3D numerical analysis of cracking and fracture of concrete materials. Fatigue Fract Eng Mater Struct 2006;29(12):979–91.
[12] Caballero A, Carol I, Lopez CM. New results in 3D meso-mechanical analysis of concrete specimens using interface elements. Comput Modell Conc Struct 2006;930:43–52.
[13] Caballero A, Lopez CM, Carol I. 3D meso-structural analysis of concrete specimens under uniaxial tension. Comput Methods Appl Mech Eng 2006;195(52):7182–95.
[14] Carol I, Bazant ZP. Damage and plasticity in microplane theory. Int J Solids Struct 1997;34(29):3807–35.
[15] Cundall PA, Strack ODL. Discrete numerical-model for granular assemblies. Geotechnique 1979;29(1):47–65.
[16] Cusatis G, Bazant ZP, Cedolin L. Confinement-shear lattice model for concrete damage in tension and compression. I. theory. J Eng Mech – ASCE 2003;129(12):1439–48.
[17] Cusatis G, Bazant ZP, Cedolin L. Confinement-shear lattice model for concrete damage in tension and compression. II. computation and validation. J Eng Mech – ASCE 2003;129(12):1449–58.
[18] Cusatis G, Bazant ZP, Cedolin L. Confinement-shear lattice csl model for fracture propagation in concrete. Comput Methods Appl Mech Eng 2006;195(52):7154–71.
[19] Cusatis G, Cedolin L. Two-scale study of concrete fracturing behavior. Eng Fract Mech 2007;74(1-2):3–17.
[20] S. Cusatis, and E.A. Schauffert, Discontinuous cell method (DCM) for cohesive fracture propagation, 2010.
[21] Delaunay BN. Sur la sphère vide. Bull. Acad. Science USSR VII: Class. Sci. Math., Bull. Acad. Sci. USSR(VII). Classe Sci Mater Nat 1934:793–800.
[22] Drucker DC, Prager W. Soil mechanics and plastic analysis for limit design. Quart Appl Math 1952;10(2):157–65.
[23] Fish J. Bridging the scales in nano engineering and science. J Nanopart Res 2006;8(5):577–94.
[24] Fuller W, Thompson SE. The laws of proportioning concrete. Trans Am Soc Civil Eng 1907:67–143.
[25] Green SJ, Swanson, SR. Static constitutive relations for concrete. Technical rept. September 1970–November 1972, 1973.
[26] Nagai K, Sato Y, Ueda T. Mesoscopic simulation of failure of mortar and concrete by 2D RBSM. J Adv Conc Technol 2004;2(3):359–74.
[27] Pelessone D. Discrete particle method. Technical report, Engineering and Software System Solutions, Inc.; September 2005.
[28] Pelessone D. MARS, modeling and analysis of the response of structures. User's manual, ES3 Inc.; 2006.
[29] Roelfstra PE, Sadouki H, Wittmann FH. Le beton numerique. Mater Struct 1985;18:327–35.
[30] Schlangen E, Van Mier JGM. Simple lattice model for numerical-simulation of fracture of concrete materials and structures. Mater Struct 1992;25(153):534–42.
[31] Si H. TetGen: A quality tetrahedral mesh generator and three-dimensional delaunay triangulator. Version 1.4. 2006. <http://tetgen.berlios.de>.
[32] Stroeven P. A stereological approach to roughness of fracture surfaces and tortuosity of transport paths in concrete. Cem Conc Compos 2000;22(5):331–41.
[33] Yip M, Li Z, Liao BS, Bolander JE. Irregular lattice models of fracture of multiphase particulate materials. Int J Fract 2006;140(1–4):113–24.